Creep and locking of a low angle normal fault: insights from the Altotiberina fault in the Northern Apennines (Italy)

L. Anderlini [1], E. Serpelloni [1], M.E. Belardinelli [2]

1 Istituto Nazionale di Geofisica e Vulcanologia, Centro Nazionale Terremoti
2 Dipartimento di Fisica e Astronomia, Settore di Geofisica, Università di Bologna

Contents of this file

Introduction

This supporting information provides additional descriptions about: 1) the GPS data processing, the velocity estimates (Text S1, Table S1 and Datasets S1 and S2) and the strain-rate analysis (Text S2 and Figure S1) discussed in Section 3, 2) the kinematic block models (Text S3 and Figure S2) and the methods used to determine the heterogeneous back-slip distribution on the ATF (Text S4 and Figures S3, S4, S5 and S6), described in Section 4, 3) the estimates of the Coulomb stressing rate (CRS) due to ATF creep-rate distribution (Text S5, Figures S7), analyzed in the Paragraph 5.2 of the main-text.

This file includes additional figures discussed in the main-text, showing the different block-model configurations tested in Section 4.1 (Figure S2), the 3D geometry of the Altotiberina fault (ATF) surface discretized in triangular dislocation elements (TDE; Figure S3), the trade-off curve used to determine the smoothing factor in the heterogeneous slip inversion (Figure S4), the sub-set of GPS sites more sensitive to the elastic deformation occurring on the ATF (Figure S5), the ATF patches interested by IC values greater than certain thresholds (Figure S6), Coulomb stress rates generated by the ATF creep-rate distribution for a specific receiver fault highlighted by the relocated microseismicity (Figure S7) and a test showing stress changes on a LANF due to a seismic rupture of hanging-wall antithetic and synthetic faults (Figure S8).

This file includes also two tables, one reporting the parameters of the rigid rotation poles for the Eurasian and Adriatic plates (TableS1) estimated using the GPS stations reported in DatasetS2 and the other reporting the statistical results (F-ratio test) of the different blocks configurations tested in Section 4 (Table S2).

The Dataset captions describe the horizontal GPS velocities used in this work in the IGS08 reference frame (DatasetS1) and the absolute velocities and residuals for the stations used to estimate the rotation poles of TableS1 (Dataset S2).

Text S1. GPS Data Processing

GPS velocities are obtained through a three step processing approach, as in Serpelloni et al. (2006; 2013). In the first step, we use daily GPS phase observations to estimate site position, adjustments to satellite orbital parameters, EOPs, and time-variable piecewise linear zenith and horizontal gradient tropospheric delay parameters using the GAMIT (V10.4) software (Herring et al., 2010), applying loose constraints to geodetic parameters. We apply the ocean-loading and pole-tide correction model FES2004 (Lyard et al., 2006), and use the Global Mapping Function (GMF) (Boehm et al., 2006) for both hydrostatic and non-hydrostatic components of the tropospheric delay model. We use the IGS absolute antenna phase centre model for both satellite and ground-based antennas. The cGPS dataset is divided into several subnets and processed independently; each subnet shares a set of high quality IGS stations, which are used as tie-stations in the second step. Survey-mode GPS networks (sGPS) are processed separately, following the same procedure adopted for cGPS data.

In the second step we use the ST_FILTER program of the QOCA software (Dong et al., 2002) to combine all the daily loosely constrained solutions, for both cGPS and sGPS subnets, with the global solutions of the IGS network made available by SOPAC (http:// sopac.ucsd.edu), and simultaneously realize a global reference frame by applying generalized constraints (Dong et al., 1998). Specifically, we define the reference frame by minimizing the velocities of the IGS core stations (http://igscb.jpl.nasa.gov), while estimating a seven-parameter transformation with respect to the GPS realization of the ITRF2008 frame (Altamimi et al., 2011), i.e., the IGS08 reference frame.

In the third step we analyze the position time series in order to estimate velocities and uncertainties (Dataset S1). For the cGPS stations we estimate a constant velocity term together with annual and semi-annual seasonal components and, if present, offsets at specific epochs. For episodic sGPS sites we only estimate the linear velocity term. We only incorporate data from cGPS stations with an observation period longer than 2.5 years, as shorter intervals may result in biased estimates of linear velocities (Blewitt and Lavallee, 2002). Following Serpelloni et al. (2013), the final velocity field is estimated from position time-series where the spatially correlated Common Mode Error (CME; Dong et al., 2006), estimated applying a principal component analysis to the residual time-series of cGPS stations at a continental scale, is removed. As a result, after removing the CME, the typical repeatability in our analysis is ~1 mm for the horizontal components, and ~3 mm for the vertical component, with

a 30% gain in the daily repeatability and a significant improvement of the signal to noise ratio. Velocity uncertainties are estimated adopting the maximum likelihood estimation (MLE) technique implemented in the CATS software (Williams, 2008), considering the presence of White noise and Flicker noise in the GPS time-series.

We use velocities from cGPS stations located on tectonically stable domains of the Eurasian plate and the Adriatic micro-plate in order to estimate their rigid rotation poles, which are reported in Table S1. The absolute velocities and residuals for the stations used to estimate the rotation poles are reported in DatasetS2.

Text S2. Continuous velocity and strain-rate fields

The final horizontal GPS velocity field (shown in Fig.1) is used to estimate the strain-rate field using a multiscale approach. We adopt the method described in Tape et al. (2009), which adopts spherical wavelets allowing the estimation of a spatially continuous velocity field on a sphere starting from a set of irregularly spaced geodetic stations. The velocity value at a given point of the Earth's surface is obtained as a superposition of values obtained at different spatial scales, than gradient quantities are directly derived from the estimated velocity field. The multiscale aspect is achieved by using wavelets from progressively finer meshes, which goes to finer scales only where justifiable, based on the GPS site density. Accordingly in the estimation we allow for short-scale spherical wavelets where GPS stations are dense, and only long-scale spherical wavelets where stations are sparse. The method allows the smallest resolved process to locally match with the local spatial density of observations.

Using Tape et al., (2009) notation, q indicates wavelets order and a corresponding spatial scale. In case of tectonic deformation fields reasonable maximum values of q ranges between 7 and 9 with corresponding scales of 55 and 14 km, respectively. The area investigated with the multiscale approach (Figure S1) allows for minimum scale wavelets (q) equal to 4 (corresponding to a spatial scale of 440 km). For almost all of the investigated area the strain-rate is resolved at a spatial scale corresponding to a $q_{max} = 9$ (corresponding to a spatial scale of 7 km), whereas $q_{max} = 10$ (corresponding to a spatial scale of 7 km) are allowed only in some spot-like areas, where the cGPS network is mush denser.

Text S3. Kinematic block modeling

We tested four different block configurations, shown in Fig. S2. Starting from models where only the ATF (model A in Fig. S2) or the Gubbio fault (model B in Fig. S2) systems accommodate the geodetic extension, we consider a model where both fault systems are active (model C in Fig. S2) and a model that accounts for extension in Tuscany (model D in Fig. S2).

Fault geometries are refined in the Umbria-Marche area, where the density of cGPS stations allows for higher spatial resolution of the deformation field (see Fig. S1), whereas all other fault segments are considered as vertical planar dislocations, locked at a depth of 10 km, except for the easternmost front of the Apennines where we consider W-dipping planes. We define the ATF segment as a ~70 km long, 15° E-

dipping plane (Chiaraluce et al., 2007), with a locking depth of 12 km (Boncio et al., 2000), and the antithetic W-dipping normal faults following the geometries proposed by Boncio et al. (2004).

We use the F-ratio test for additional plate boundaries (Stein and Gordon, 1984) to evaluate whether more complex models, giving lower χ^2 values, are statistically significant (see Tab. S2). The lowest residuals (reduced χ^2=1.99) are provided by the most complex model (model D in Fig. S2).

Text S4. Analysis of the back-slip distribution on the ATF

We discretize the non-planar surface of the ATF (Fig. S3), as obtained following the depth contour isobaths proposed by Mirabella et al. (2011), into triangular dislocation elements (TDEs) using the GMSH software (Geuzaine and Remacle, 2009), whose result is shown in Figure S3.

We use a constrained linear least squares inversion scheme, based on the preconditioned conjugate gradient method (Coleman and Verma, 2001), bounding the down-dip ATF back-slip values to be lower than the ATF long-term geodetic slip-rate, V_0, estimated in model D (V_0=1.7 mm/yr). We constrain the slip-rate to taper to zero at the bottom of the ATF surface, at a depth of ~13 km, roughly corresponding to the proposed brittle-ductile transition for this region (Boncio et al., 2004).

The underdetermined solution is regularized using a Laplacian operator weighted by a smoothing factor (β), which controls the relative importance of minimizing the residuals versus minimizing the roughness of the back-slip distribution (as in Meade and Loveless, 2009). We choose an optimal value of $\beta = 0.5$ from a trade-off curve analysis (e.g. Harris and Segall, 1987), as shown in Figure S4.

Text S5. Coulomb stressing rate estimate

We use the Nikkhoo and Walter (2015) code for triangular dislocation sources in order to estimate the static stressing rate tensor, $\boldsymbol{\sigma}_{nr}$, generated by the ATF creep distribution. We use as Lamé parameters $\lambda = 40$ GPa and $\mu = 30$ GPa, estimated from the 1D velocity model proposed in Carannante et al. (2013) and assuming an average density of 2650 kg/m3 (Collettini, 2002).

We compute the Coulomb stress rate (CSR, e.g. King et al., 1994) defined as:

$$CSR = \tau_r + \mu_e \cdot \sigma_{nr}$$

where τ_r is the shear stress rate, σ_{nr} is the normal stress rate (positive for extension) and μ_e is the effective friction coefficient that we assume equal to 0.4. Note that this choice is not affecting significantly results of Fig. 2c of the maintext, since the normal stress variation tends to vanish on the source fault surface, if evaluated for a receiver fault equal to the source fault, as it is in Fig. 2c (see e.g. Fig. 2a of King et al., 1994).
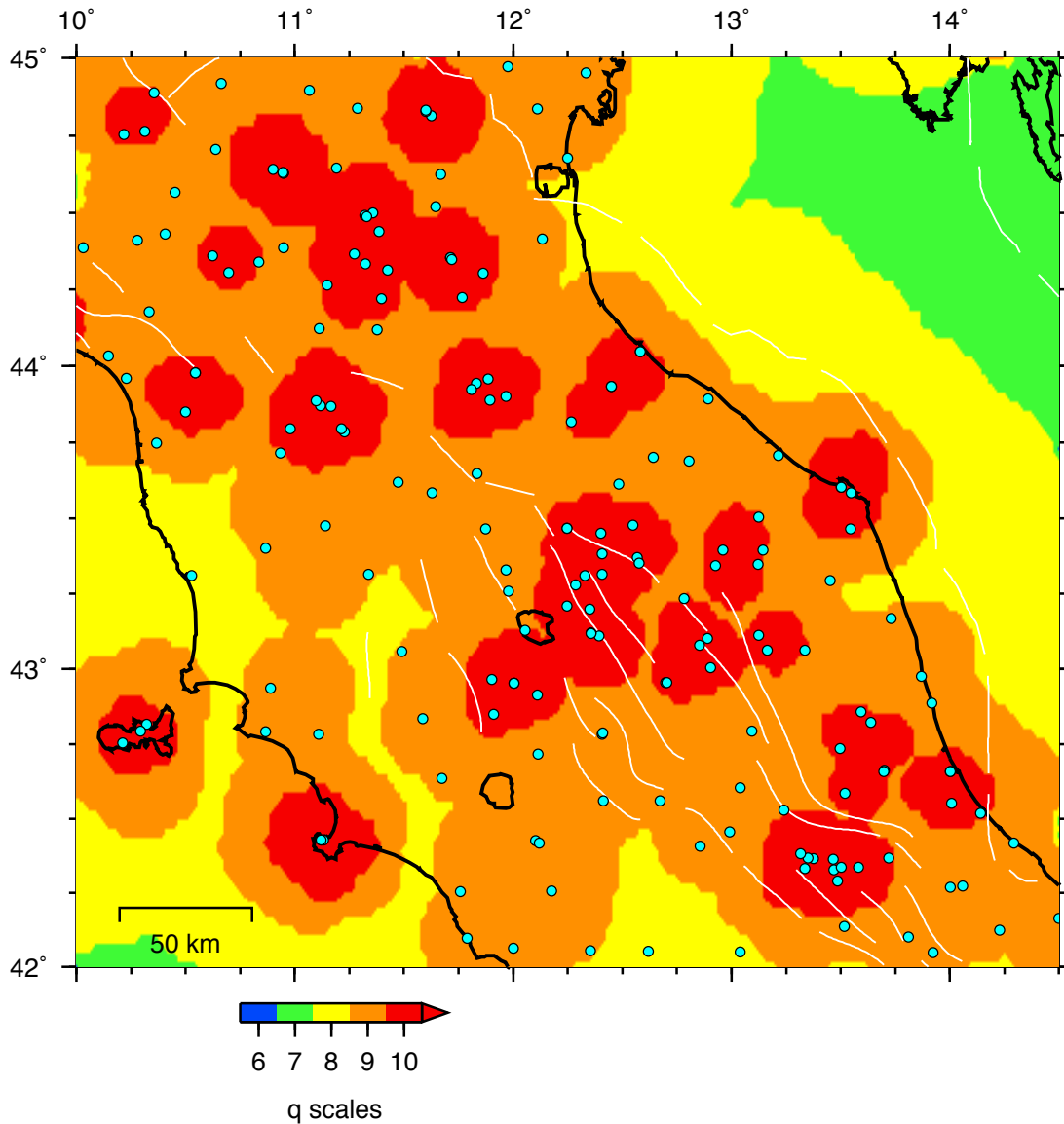
Figure S1. Selected maximum values of spherical-wavelets orders based on the GPS station distribution (cyan circles). The interval q = 4–10 is considered (only the 6-10 interval is shown in figure). The density of the observation points controls the selection of spherical wavelets, whose center points are not shown. The color map shows the maximum-q scale wavelet that covers each area where the coverage is determined by the length scale for each spherical wavelet. Where stations are dense, wavelets with all scales q = 4–10 (red) are available; where stations are sparse, only wavelets with longer length scales q = 4–9 (orange) are available.
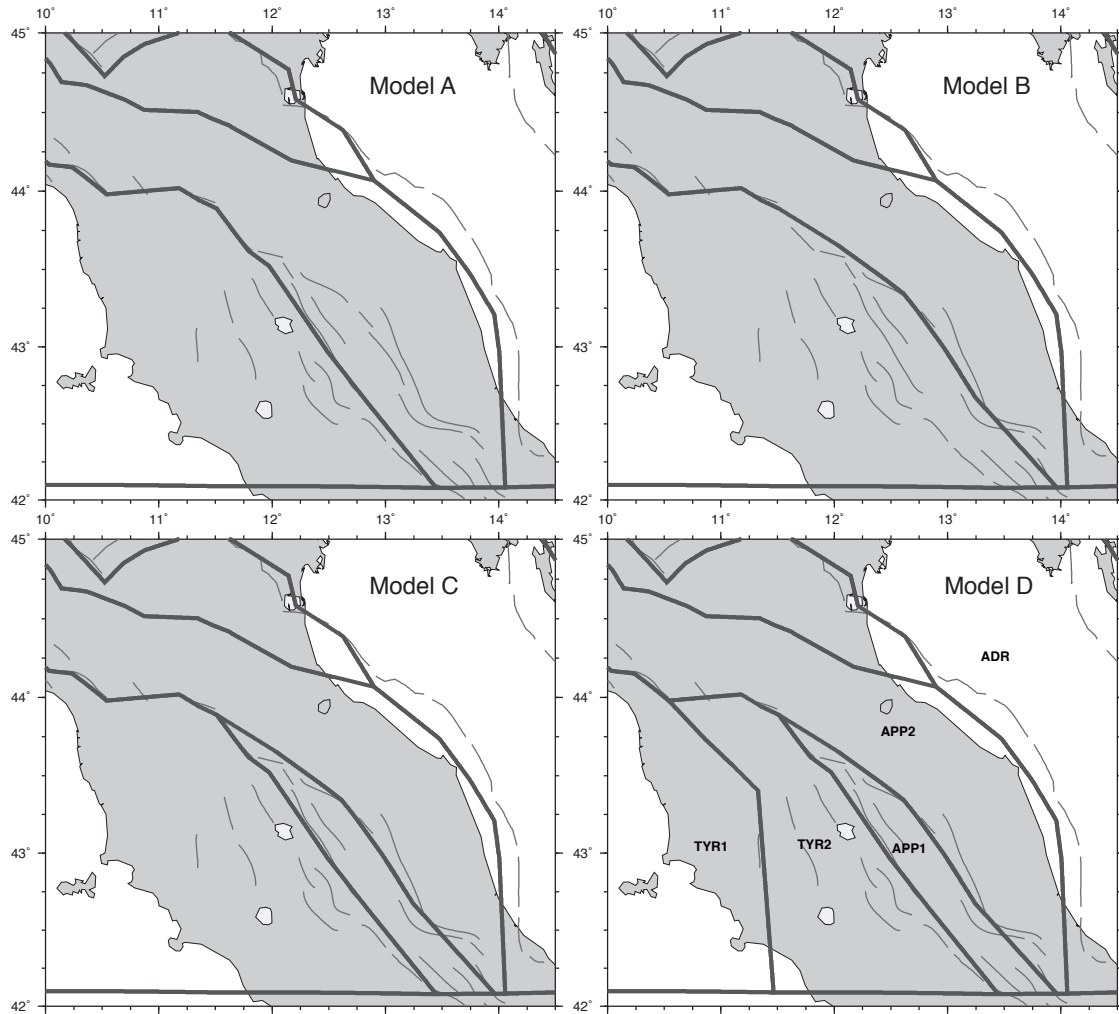
Figure S2. Geometries of the block models tested in this work (see Table S2). Models A and B are the simplest ones, where only the ATF or the west-dipping normal fault system (Gubbio fault system), respectively, are assumed to accommodate geodetic extension. In Model C both fault systems are active, whereas Model D accounts for extension in Tuscany. Model D provides the lowest residuals while passing the F-test for additional blocks (see Table S2 and main-text.).
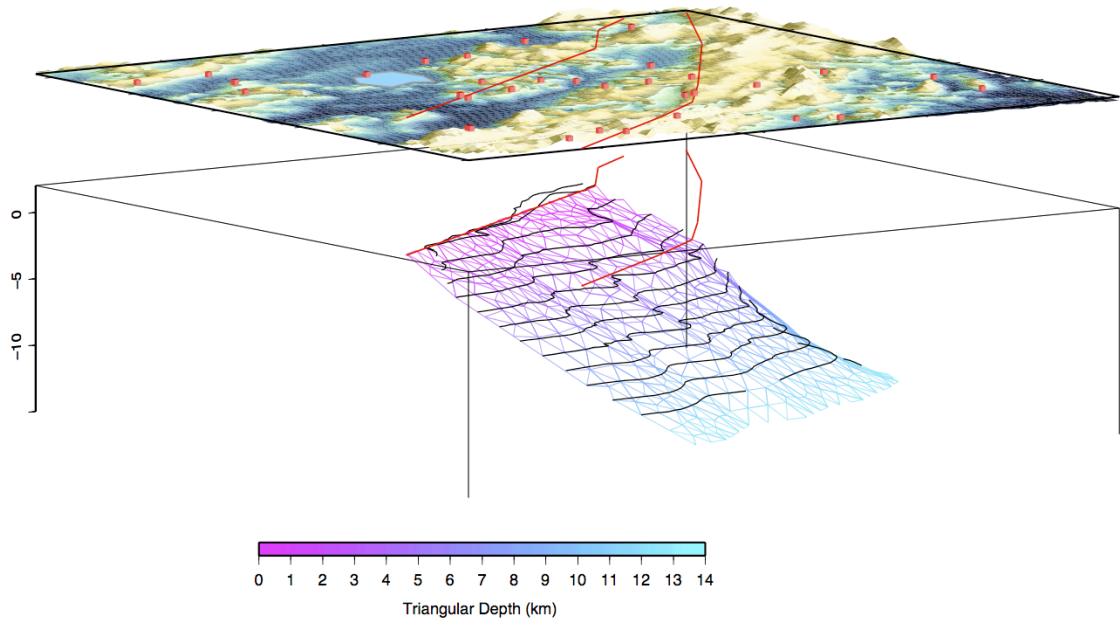
Figure S3. 3D view of the curved Altotiberina surface, obtained following the depth contour isobaths proposed by Mirabella et al. (2011) (black lines). The surface is discretized into triangular dislocation elements (TDE) with a mean surface of 3.5 km^2 using the GMSH software (Geuzaine and Remacle, 2009). In particular it is discretized into 754 TDEs deepening down to 13 km of depth, corresponding to the brittle-ductile transition from Boncio et al. (2004). The red lines show the APP1 block-bounding fault traces (Fig. S2) and the GPS stations are indicated by red squares.
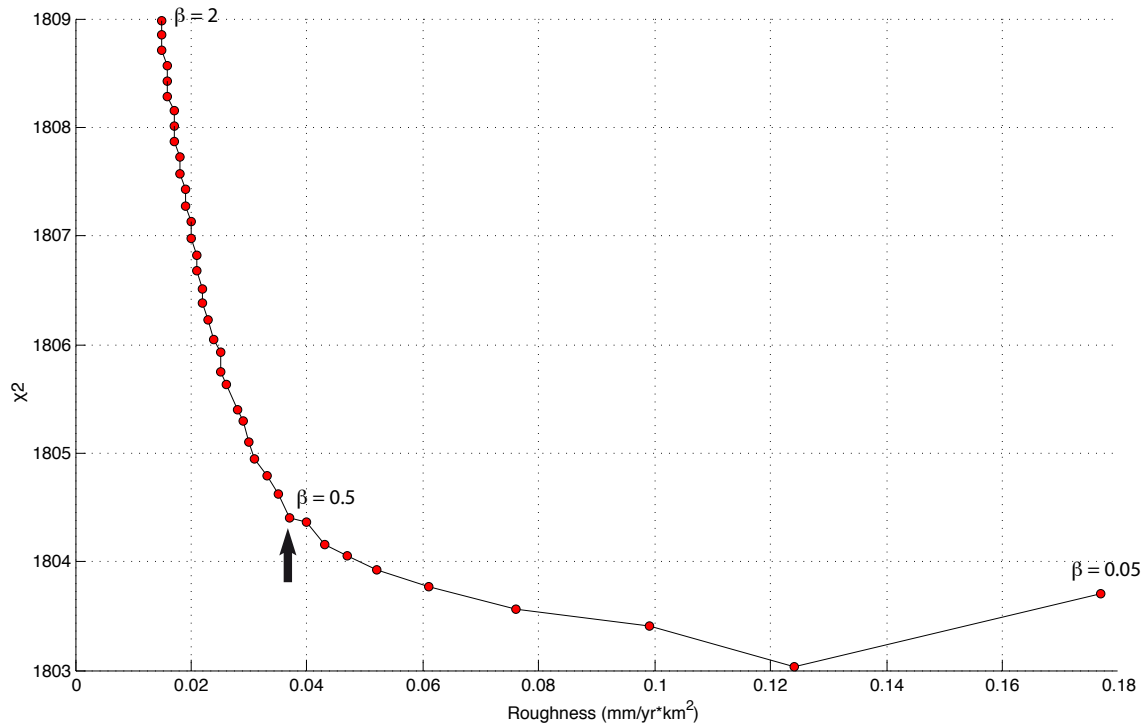
Figure S4. Trade-off curve between the fault-slip model roughness and the misfit function (χ^2) for several β values used to weight the smoothing constraint on the back-slip distribution. We evaluated these quantities with β values starting from 0.05 to 2 with steps of 0.05 and we chose the optimal one (β=0.5) following the approach of Harris & Segall (1987).
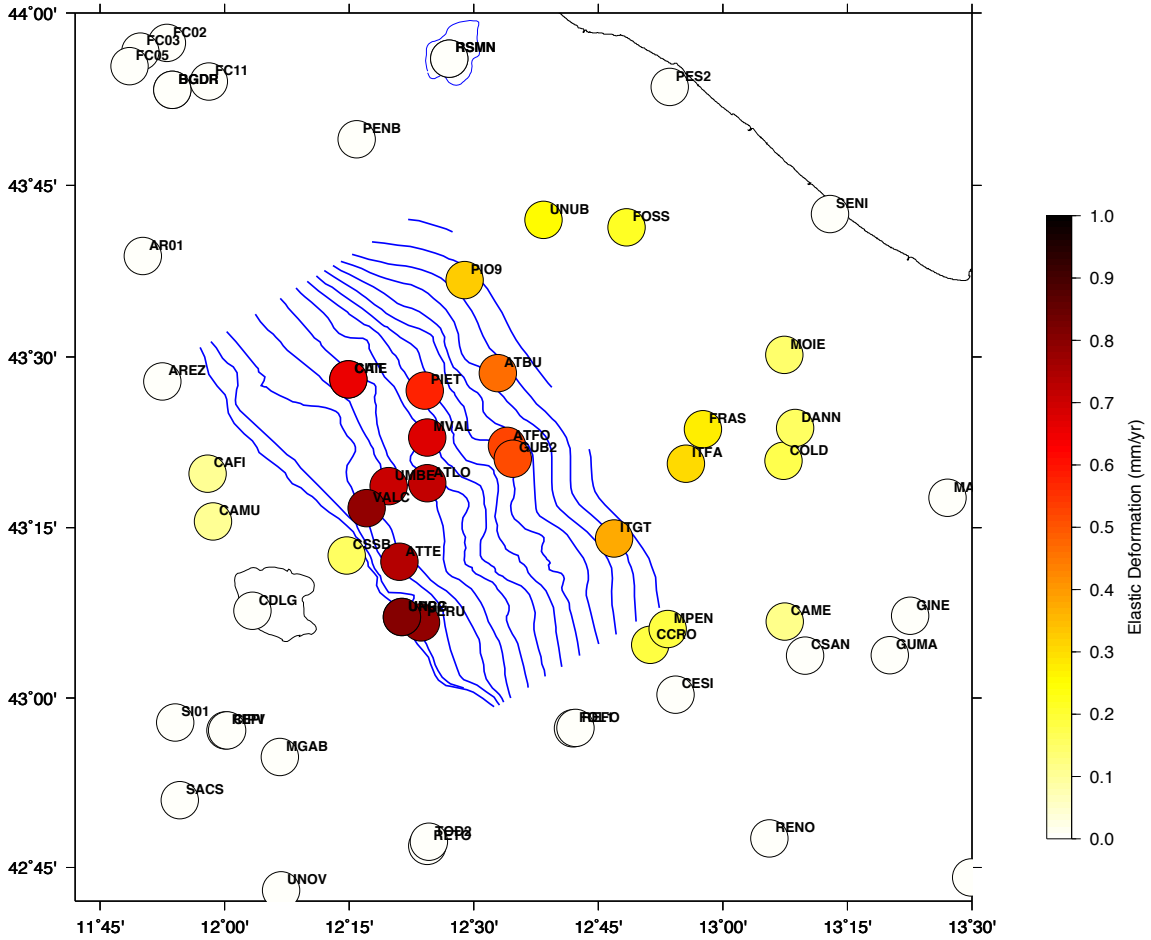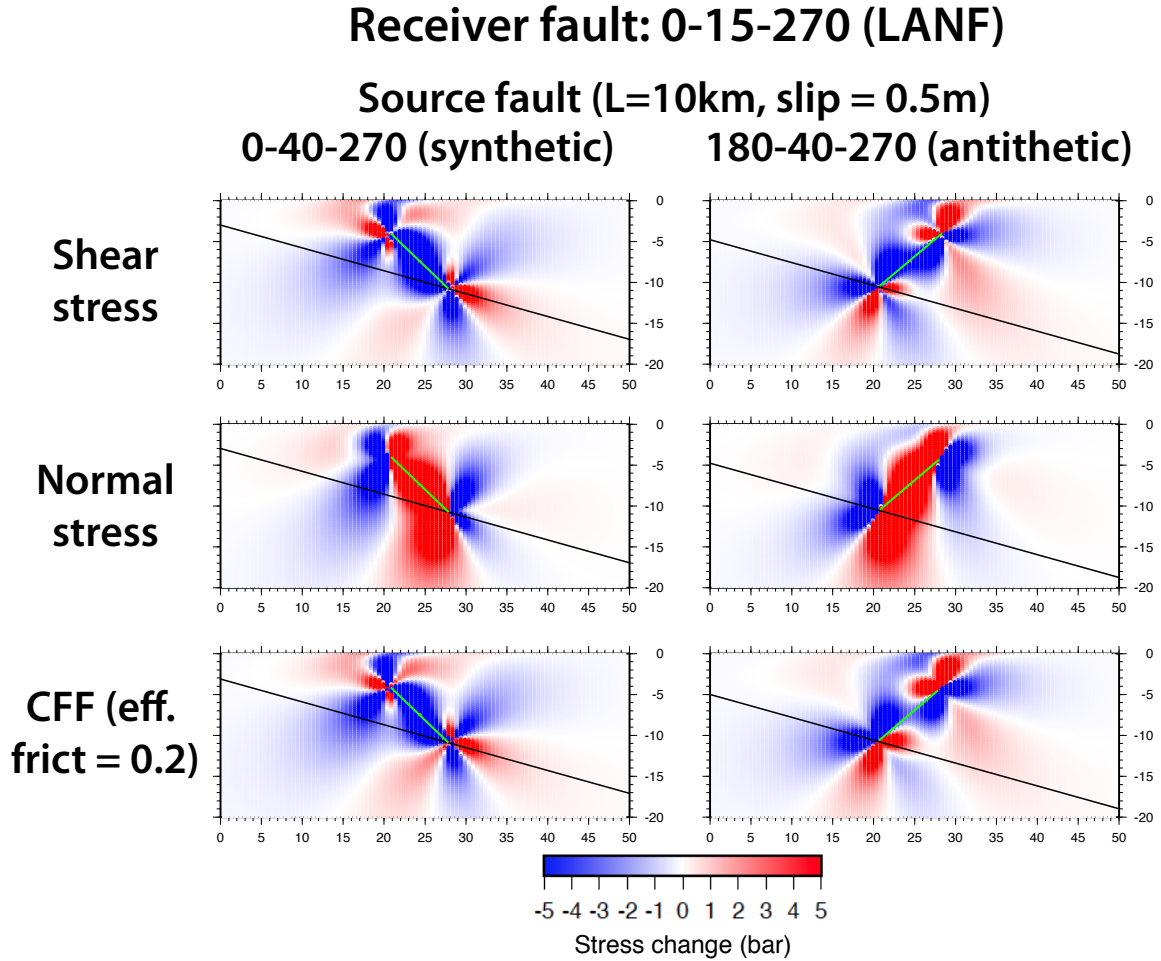
Figure S5. Velocity estimates at GPS stations close to the ATF, when 1 mm/yr dip slip rate is assigned to each TDE of the ATF (Fig. S3). Circles are colored if the GPS station velocity is larger than 0.1 mm/yr.
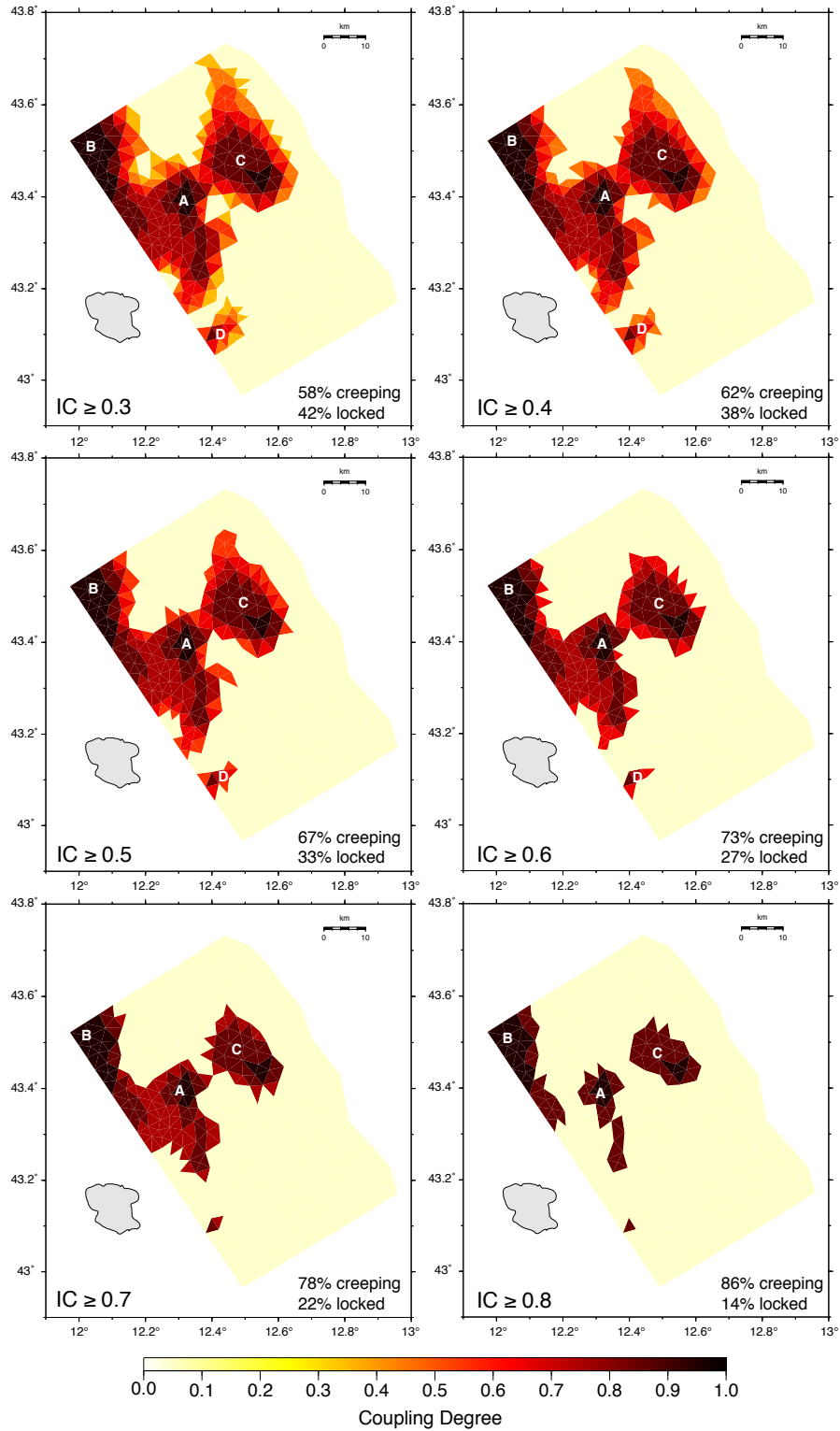
Figure S6. ATF surface patches with interseismic coupling (IC) values above a certain threshold c_t, starting from 0.3 up to 0.8. For each case the percentage of "locked" (IC ≥ c_t) and "creeping" (IC < c_t) surface is indicated. A-B-C-D letters indicate separate asperities that become more evident with high threshold values.
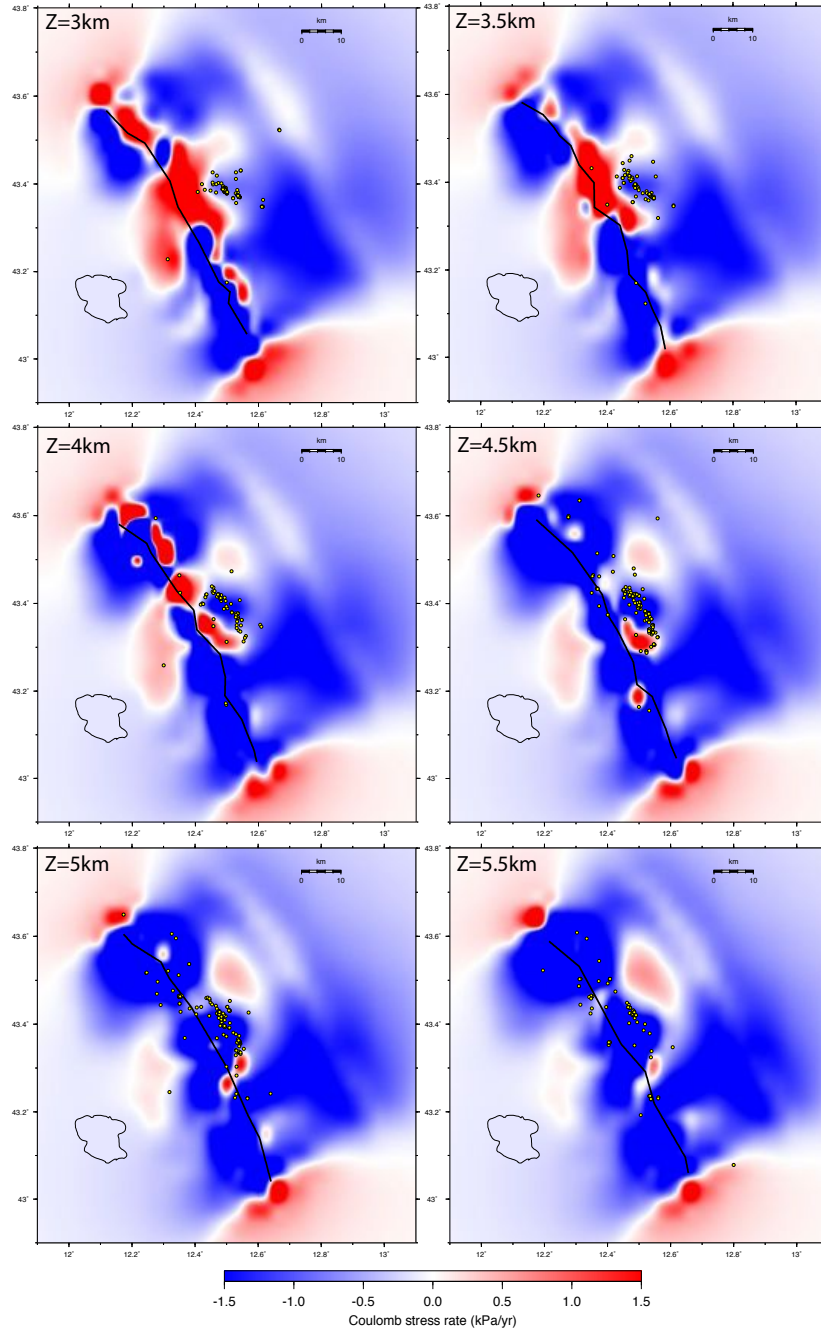
Figure S7. Maps of the Coulomb stressing rate (CSr) due to the ATF creep-rate distribution (Fig. 3a) calculated at different depths in the crustal volume surrounding the ATF. We consider a receiver fault mechanism with strike = 140°, dip = 60° (constant in the Figure) corresponding to an antithetic normal fault identified by the micro-seismicity relocated in the ATF hanging wall (Chiaraluce et al., 2007). In each sub-plot the black line indicates the trace of the ATF surface intersected at the correspondent depths and the yellow dots shows the relocated microseismicity whose hypocentral depth is no further away of 200 m from the depth layer. The used rheological parameters (λ, μ, density and effective friction coefficient) are reported in text S5.

Receiver fault: 0-15-270 (LANF)

Source fault (L=10km, slip = 0.5m)
0-40-270 (synthetic)   180-40-270 (antithetic)

Figure S8. Cross section through a LANF plane (black lines) showing the stress changes generated by 0.5 m of uniform slip occurred on blind synthetic (left) and antithetic (right) faults (green lines) with a length of 10 km, assuming as a receiver fault the same LANF (whose fault mechanism: strike, dip and rake (°), is indicated in the figure title). On top of each column the strike, dip and rake (°) of the source fault are indicated. An effective friction μ_e=0.2 is assumed. The assumed elastic parameters are reported in Text S5.

Pole:	lat	s(lat)	lon	s(lon)	corre	omega	S(ome)
EUR	55.99	0.25	-97.55	0.23	0.1272	0.262	0.001
ADR	62.09	3.22	-28.22	0.79	0.0971	0.508	0.006
ADR-EUR	45.06	3.01	8.18	1.21	-	0.3254	0.0073

Table S1. Absolute and relative rotation poles of the Eurasian and Adriatic rigid plates estimated using the GPS stations reported in DatasetS2. The table reports latitude (lat), longitude (lon) and associated errors (s(lat) and s(lon)) in degrees, the related correlation (corre) and the rotation rates (omega) with the corresponding uncertainties (S(ome)) in deg/Myr.

Model name	Chi2	n. Blocks	F-test	$F_{99\%}$
Model A	2317.29	10	-	-
Model B	2293.77	10	-	-
Model C	2217.25	11	**A -> C**: 13.82 **B -> C**: 10.57	3.81
Model D	1825.01	12	**C -> D**: 65.62	3.81

Table S2. Results of the F-test obtained from different block configurations shown in Fig. S2. The second and third columns show the chi2 values and the number of blocks for each model, respectively. The fourth column shows the F-test values (positive if greater than 3.81 with a confidence level up to 99% (Stein and Gordon, 1984) obtained considering the four model settings. For Model A the dip-slip rate of the ATF is 2.6±01 mm/yr. For Model B the dip-slip rate of the Gubbio fault is 3.2±0.1 mm/yr. For Model D the dip-slip rates of the ATF and Gubbio faults are 1.7±0.3 mm/yr and 1.5±0.3 mm/yr, respectively

Data Set S1. GPS horizontal velocities (in mm/yr) in the IGB08 reference frame. Activity time interval and 1σ uncertainties are also reported.

Data Set S2. GPS horizontal velocities (in mm/yr with 1σ uncertainties) in the IGB08 reference frame for the stations used to estimate the rigid rotation poles of Eurasia and Adria plates. Velocity residuals for east and north components and for the amplitude and azimuth (°N) are also reported.

References

Altamimi, Z., X. Collilieux, and L. Métivier (2011), ITRF2008: an improved solution of the international terrestrial reference frame, J Geodesy, 85(8), 457–473, doi:10.1007/s00190-011-0444-4.

Blewitt, G. and D. Lavallée (2002), Effect of annual signals on geodetic velocity, J. Geophys. Res., 107(B7), 2145, doi:10.1029/2001JB000570.

Boehm J., A. Niell, P. Tregoning, and H. Schuh (2006), Global Mapping Function (GMF): A new empirical mapping function based on numerical weather model data, Geophys. Res. Lett., 33, L07304. doi:10.1029/2005GL025546.

Boncio, P., F. Brozzetti, and G. Lavecchia (2000), Architecture and seismotectonics of a regional low-angle normal fault zone in central Italy, Tectonics, 19, 1038–1055, doi: 10.1029/2000TC900023.

Boncio, P., G. Lavecchia, and B. Pace (2004), Defining a model of 3D seismogenic sources for Seismic Hazard Assessment applications: The case of central Apennines (Italy), J. Seismol., 8, 407–425, doi:10.1023/ B:JOSE.0000038449.78801.05.

Carannante, S., G. Monachesi, M. Cattaneo, A. Amato, and C. Chiarabba (2013), Deep structure and tectonics of the northern-central Apennines as seen by regional-scale tomography and 3-D located earthquakes, J. Geophys. Res. Solid Earth, 118, 5391–5403, doi:10.1002/jgrb.50371

Chiaraluce, L., C. Chiarabba, C. Collettini, D. Piccinini, and M. Cocco (2007), Architecture and mechanics of an active low-angle normal fault: Alto Tiberina Fault, northern Apennines, Italy, J. Geophys. Res., 112, B10310, doi:10.1029/2007JB005015

Coleman, T.F., and A. Verma (2001), A preconditioned conjugate gradient approach to linear equality constrained minimization, Comput. Optim. Appl., 20(1), 61–72, doi:10.1023/A:1011271406353.

Collettini, C. (2002), Hypothesis for the mechanics and seismic behaviour of low-angle normal faults: the example of the Altotiberina fault Northern Apennines, Annals of Geophysics, 45(5), 683-698.

Dong, D., T. Herring, and R. King (1998), Estimating regional deformation from a combination of space and terrestrial geodetic data, J. Geodesy, 72(4), 200–214.

Dong, D., P. Fang, Y. Bock, M. Cheng, and S. Miyazaki (2002), Anatomy of apparent seasonal variations from GPS-derived site position time series, J Geophys Res-Sol Ea, 107, –, doi:10.1029/2001JB000573.

Dong, D., P. Fang, Y. Bock, F. Webb, L. Prawirodirdjo, S. Kedar, and P. Jamason (2006), Spatiotemporal filtering using principal component analysis and Karhunen-Loeve expansion approaches for regional GPS network analysis, J. Geophys. Res., 111, B03405, doi:10.1029/2005JB003806.

Geuzaine, C. and J.-F. Remacle, (2009), Gmsh: a three-dimensional finite element mesh generator with built-in pre- and post-processing facilities. International Journal for Numerical Methods in Engineering 79(11), pp. 1309-1331

Harris, R.A. and P. Segall (1987), Detection of a locked zone at depth on the Parkfield, California, segment of the San Andreas Fault, J. geophys. Res., 92, 7945–7962.

Herring, T., R.W. King and S. McClusky (2010), GAMIT Reference Manual, Release 10.4, Massachussetts Institute of Technology, Cambridge, MA.

King, G.C.P., R.S. Stein and J. Lin (1994), Static Stress Changes and Triggering of Earthquakes, Bull. Seismol. Soc. Am., 84 (3), 935-953.

Lyard, F., F. Lefevre, T. Letellier, and O. Francis (2006), Modelling the global ocean tides: Modern insights from FES2004, Ocean Dynam., 56, 394–415.

Meade, B.J., and J.P. Loveless (2009), Block modeling with connected fault-network geometries and a linear elastic coupling estimator in spherical coordinates, Bull. Seismol. Soc. Am., 99, 3124–3139, doi:10.1785/0120090088.

Mirabella, F., F. Brozzetti, A. Lupattelli, and M. R. Barchi (2011), Tectonic evolution of a low - angle extensional fault system from restored cross - sections in the Northern Apennines (Italy), Tectonics, 30, TC6002, doi:10.1029/2011TC002890.

Nikkhoo, M. and T. R. Walter (2015), Triangular dislocation: an analytical, artefact-free solution, Geophys. J. Int. 201, 1117–1139. doi: 10.1093/gji/ggv035.

Serpelloni, E., G. Casula, A. Galvani, M. Anzidei, and P. Baldi (2006), Data analysis of permanent GPS networks in Italy and surrounding regions: Application of a distributed processing approach, Ann. Geophys.-Italy, 49, 897–928.

Serpelloni, E., C. Faccenna, G. Spada, D. Dong, and S. D. P. Williams (2013), Vertical GPS ground motion rates in the Euro-Mediterranean region: New evidence of velocity gradients at different spatial scales along the Nubia-Eurasia plate boundary, J. Geophys. Res. Solid Earth, 118, 6003–6024, doi:10.1002/2013JB010102.

Stein, S. and R. Gordon (1984), Statistical test of additional plate boundaries from plate motion inversion. Earth Planet. Sci. Lett, 69, 401-412.

Tape, C., P. Musé, M. Simons, D. Dong, and F. Webb (2009), Multiscale estimation of GPS velocity fields, Geophys. J. Int., 179(2), 945–971, doi:10.1111/j.1365-246X.2009.04337.x.

Williams, S. D. P. (2008), CATS: GPS coordinate time series analysis software, GPS Solut., 12(2), 147–153, doi:10.1007/s10291-007-0086-4.